Korean J. Chem. Eng., 33(7), 2228-2234 (2016)
DOI: 10.1007/s11814-016-0036-3

pISSN: 0256-1115
eISSN: 1975-7220

Hierarchically nanostructured carbon-supported manganese oxide for high-performance pseudo-capacitors

Xinhua Huang*, Miri Kim, Hongsuk Suh***, and Il Kim**,†**

*School of Materials Science and Engineering, Anhui University of Science and Technology, Huainan 232001, China
**BK21 PLUS Centre for Advanced Chemical Technology, Department of Polymer Science and Engineering, Pusan National University, Busan 46241, Korea
***Department of Chemistry and Chemistry Institute for Functional Materials, Pusan National University, Busan 46241, Korea
(*Received 13 November 2015 • accepted 30 January 2016*)

Abstract−We developed 3-D network carbon materials by directly pyrolyzing as-prepared polynaphthalene (PNT). The PNT-based materials were synthesized from chloromethylated naphthalene and were self-polymerized using anhydrous aluminum chloride as the Friedel-Crafts catalyst and chloromethyl methyl ether as a crosslinker. The micro-, meso-, and macroporous 3-D carbon materials showed large specific surface areas, large electrolyte-electrode interface areas, and continuous electron transport paths. MnO_2/carbon composites were then synthesized by chemically depositing MnO_2 onto the carbon substrate surfaces through a self-limiting redox reaction between $KMnO_4$ solution and carbon substrates, producing high-performance *pseudo*-capacitor electrodes. The unique electrode architecture demonstrated high capacitance up to 286.8 F g^{-1}, and good cycling stability up to 1000 cycles without losing its capacitance. The electrode shows potential applications for the development of high-performance supercapacitors for a variety of power-demanding devices.

Keywords: Capacitor, Carbon Materials, Composite, Metal Oxide, Network Structure, Polynaphthalene

INTRODUCTION

Supercapacitors (or electrochemical capacitor, electrical double-layer capacitor) are popular and effective for electrochemical energy storage, with batteries having broader market access. They have broad usage such as cranes, vehicles, martial tanks and laser weapons. Pseudo-capacitance resulting from the redox reaction between electrode materials and electrolytes, accumulating electrons at the electrode is a fast Faradic reaction, which is typically ten-times stronger than electric double layer capacitance [1,2]. Metal oxides such as RuO_2, MnO_2, NiO, Co_3O_4, TiO_2, and V_2O_5 [3-8] are being utilized for supercapacitor (SC) electrodes to improve specific capacitance and energy density. For example, an electrodeposited NiO thin film electrode showed a specific capacitance of 1,776 F g^{-1} in 1 M aqueous KOH electrolyte when the electrode was scanned at 1 mV s^{-1}. However, the electrode only retained 23% of its capacitance when it was scanned at 100 mV s^{-1} [9]. Therefore, metal oxides may not be used alone as SC electrodes because the conductivity of most metal oxides except RuO_2 is very low, the strain developed in the pure metal oxide during charging/discharging causes the electrode to crack, leading to poor long-term stability, and the surface area, pore distribution, and porosity are difficult to tailor in metal oxides [10].

These nanomaterials are currently being engineered to overcome the drawback of slow ion and electron diffusion in conventional electrodes [4,11,12]. It is logical to develop a composite electrode containing both commercial capacitive carbon and low-cost *pseudo*-capacitive metal oxides, which can potentially offer cost advantages and high performance by combining the advantages and mitigating the disadvantages each component [13]. In carbon nanostructure/metal oxide composite electrodes, the carbon nanostructures not only serve as the physical support of the metal oxides but also provide the channels for charge transport [10], and the metal oxides mainly store the charge and energy.

To prepare carbon/metal oxide composites, many researchers have used graphene oxide composited with metal oxide as a hybrid structure to enhance the specific capacitance and energy density of electrodes [14-19]. A few researchers have even developed carbon structures to fabricate new carbon/metal oxide composites (see Table 1). Lu et al. developed hierarchical MnO_2/carbon nanocomposites showing high specific capacitance and excellent rate capability [20]. Therefore, it is highly desirable to develop more mesoporous carbon substrates to fabricate composite electrodes.

The structure of the carbon substrate is an important factor that affects the electrochemical performance. For example, physical properties of the substrate such as morphology and microstructure, surface area, and pore size affect the nature of the deposited metal oxide as well as the electrochemical properties of the final hybrid device [21]. Thus, three-dimensional (3-D) carbon nanostructures bearing lower-dimensional building blocks and retaining their original advantages are promising candidates for supporting metal oxides [10]. When used in SC electrodes, such 3-D car-

†To whom correspondence should be addressed.
E-mail: ilkim@pusan.ac.kr

Table 1. Summary of recently synthesized carbon/metal oxide composite-based electrodes

Samples	C_s[c] (F/g)	Features	Ref.
Hierarchical porous carbon-MnO_2	218 (0.1 A/g)	High C_s and excellent capability	[20]
Tubular mesoporous carbon-SnO_2	127 (0.3 A/g)	High energy density	[22]
Carbon black-MnO_2	183 (2 mV/s)	Higher C_s	[23]
Carbon fiber-Nanonet/Nanoflower NiO	840 (1 mA/cm^2)	Much-improved areal capacitance	[24]
Activated carbon-$NaMn_{1/3}Ni_{1/3}Co_{1/3}PO_4$	45 (0.5 A/g)	Reversibility	[25]
Carbon nanosheets-MnO	1332[a] mAh/g (0.1 A/g)	High energy and very long time cycle ability	[26]
SCNTs-activated carbon-V_2O_5	>1000 (0.1 A/g)	High specific pseudo-capacitance	[27]
[b]PEDOT/MnO_2/MWCNTs	157 (30 mV/s)	Improved rate capability	[28]

[a]Energy density
[b]Poly(3,4-ethylenedioxythiophene)-MnO_2/multiwall carbon nanotubes
[c]Specific capacitance

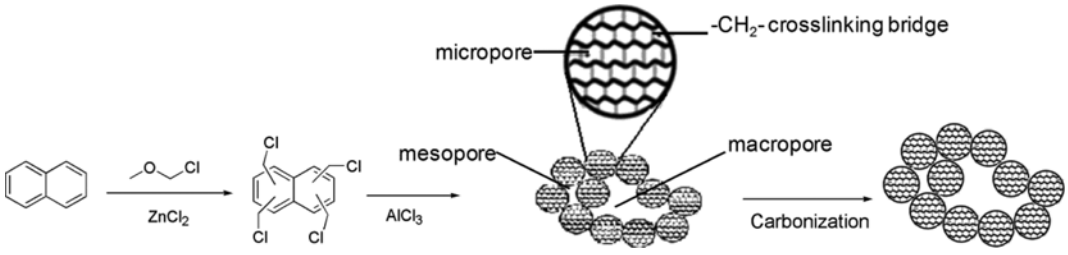

Fig. 1. Schematic illustrating synthesis of as-prepared polyaromatic hierarchical structure and carbon materials.

bon nanostructures show large specific surface areas, large electrolyte-electrode interface areas, and continuous electron transport paths.

In our study, we synthesized a new hypercrosslinked polynaphthalene (PNT) by self-condensation the chloromethylation of naphthalene. After pyrolysis of PNT, the carbon materials from naphthalene were prepared as predominantly micro-, meso-, and macroporous structures that have large surface areas. Such hierarchical pore structure provides a suitable ion transport channel and active pore walls, increasing the specific capacitance (Fig. 1). Hence the PNT carbon support offers a platform for 3-D pore structure and the high specific surface area in the metal oxide-carbon electrodes. MnO_2/carbon composites were then synthesized using chemical deposition through a spontaneous self-limiting redox reaction with $KMnO_4$ solution at 50 °C [20] given as follows:

$$4MnO_4^- + 3C + 2H_2O \rightarrow 4MnO_2 + 3CO_2 + 4OH^- . \quad (1)$$

As a *pseudo*-capacitive electrode material, MnO_2 has attracted considerable interest because it shows a high theoretical specific capacitance (1,370 F g^{-1}) and is inexpensive and environmentally benign [29]. The activity of manganese oxides relies heavily on their chemical composites and crystallographic structure, as well as morphologies and pore structure [30]. The pseudo-capacitor fabricated using the HPN-supported hybrid electrode demonstrated significantly improved electrochemical use of the active materials (*i.e.*, high mass loading) for efficient charge storage. The hybrid electrode demonstrated high areal capacitance and capacitance retention. Such a hybrid-structured capacitor also exhibited a long-term cycling performance after over 1000 charge-discharge cycles.

EXPERIMENTAL

1. Materials

The methylene crosslinking bridges between the naphthalene (NT; 98%) molecules were produced using CME (95%) and zinc dichloride ($ZnCl_2$, 98%). Anhydrous aluminum chloride ($AlCl_3$, 98%, JUNSEI) was used as the Friedel-Crafts catalyst, and sodium sulfate (Na_2SO_4, 98%) was diluted to a concentration of 1 M and used as the electrolyte. All of these materials were purchased from Sigma-Aldrich except for the $AlCl_3$. The $ZnCl_2$ was dried at 110 °C under vacuum before being used. Potassium permanganate ($KMnO_4$, 99%) was purchased from Hayashi Pure Chemical Industries, Ltd., and 1,2-dichloroethane (DCE) was purchased from DAEJUNG Chemicals Company and was distilled before use. Poly(vinylidene fluoride) (PVDF), whose average molecular weight was 534,000, as determined using gel permeation chromatography (GPC), was purchased from Sigma-Aldrich, carbon black was purchased from VULCAN XC72 COBOT CORPORATION, and *N*-methyl-2-pyrrolidinone (NMP, 98%) was purchased from Sigma-Aldrich.

2. Synthesis of Carbonized Polynaphthalene (PNT-C)

NT (1 g, 7.8 mmol), CME (2.52 g, 31.0 mmol), and $ZnCl_2$ (1 g, 7.3 mmol) were dissolved in 10 mL of DCE in a 50-mL flask equipped, and the mixture was stirred at 40 °C for 12 h under $N_2$for chloromethylation [31]. The solvent was then evaporated by distillation at 40 °C, and the residue was washed with water three times to remove the inorganic residue. The chloromethylated product, NT-CME4, was dried under vacuum at room temperature to give a light-green powder, yielding 71%.

The obtained NT-CME4 was dissolved in 60 mL of DCE in a

Table 2. Detailed properties of carbon and composite electrodes

Sample	$C^a_{MnO_2}$ (wt%)	SA^b (m^2/g)	C_s^c (F/g)	ESR^d (Ω)
Carbon	0	711.6	86.7	0.94
C-MnO_2-10	29	514.3	144.5	6.26
C-MnO_2-30	50	395.7	196.3	9.10
C-MnO_2-60	71	307.1	202.5	9.34
C-MnO_2-120	81	211.5	286.8	22.06

[a]MnO_2 content of samples
[b]Surface area
[c]Specific capacitance according to the charge-discharge curves under 100 mA/g
[d]Equivalent series resistance

100-mL flask equipped with a reflux condenser. Slurry consisting of $AlCl_3$ (1 g, 7.5 mmol) dissolved in 5 mL of CME was added to the flask, and the mixture was self-polymerized at 80 °C for 12 h. The resulting precipitate was washed well with water and methanol until the filtrate was clear. The polymer was then dried under vacuum for 8 h at 80 °C and extracted using a Soxhlet extractor and methanol for 24 h. The desired polynaphthalene (PNT) polymer was collected (95% yield) and dried overnight in a vacuum oven at 110 °C. The obtained PNT was then pyrolyzed in a quartz tube at 600 °C for 5 h, heated at 10 °C min^{-1} under high purity N_2 flowing at 30 cm^3 min^{-1}, and left in the furnace as it naturally cooled to room temperature to produce PNT-C (see Fig. 1).

3. Synthesis of MnO_2/PNT-C Composites

The MnO_2/carbon composite was synthesized using a procedure adapted from the literature [32]. Briefly, 0.08 g samples of carbon substrate were soaked in 25 mL of Na_2SO_4 solution (0.1 M) at 50 °C and were stirred with a 25-mL solution containing 0.1 M $KMnO_4$ and 0.1 M Na_2SO_4 for 10, 30, 60, or 120 min. The products were then washed with deionized water and dried at 80 °C under vacuum for 24 h; the products are denoted C-MnO_2-time (*e.g.*, C-MnO_2-120, in Table 2).

4. Material and Electrode Characterization

X-ray diffraction (XRD; automatic Philips powder diffractometer with nickel-filtered Cu Kα radiation) was used to determine the crystallinity of the electrode materials. The diffraction patterns were generated in the range 2θ=10-70° in 0.02° steps at 2 s $step^{-1}$. The Brunauer-Emmett-Teller (BET) surface area (S_{BET}) was determined using BET theory. The total pore volumes (V_t), estimated from the amount of nitrogen adsorbed at a relative pressure (P/P_0) of ~0.997 at 77 K, were measured on a Nova 3200e system (Quantachrome Instruments, USA). The pore size distribution was analyzed using the Barrett-Joyner-Halenda (BJH) method combined with nonnegative regularization and medium smoothing. The microstructures of the samples were investigated by scanning electron microscopy (SEM; S-4800, Hitachi, Japan) and high-resolution transmission electron microscopy (HRTEM, JEM-2100F, USA). The MnO_2 content was estimated by inductively coupled high-frequency plasma spectrometry (ICP, ELAN DCR-e, Perkin Elmer, USA).

The electrodes were assembled on nickel foam collectors [33]. Briefly, 75 wt% of the test materials, 20 wt% of carbon black, and 5 wt% of PVDF dispersed in NMP were mixed to form slurry, which was then ultrasonicated at 60 °C for 30 min, coated onto the nickel foam, and dried at 60 °C for 6 h. The electrochemical performance of SCs was characterized using a classical three-electrode configuration (INIUM VERTEX. 1A) in 1 M aqueous Na_2SO_4 at room temperature. A platinum wire and an Ag/AgCl electrode were used as the counter and reference electrodes, respectively. The cyclic voltammetry (CV) curves were scanned in the range 0-0.9 V at different rates, and the cell was galvanostatically charged/discharged in the range 0-0.9 V at different current densities. Electrochemical impedance spectroscopy (EIS) measurements were recorded under an alternating current (AC) voltage amplitude of 5 mV, a frequency range of 10^5 to 0.1 Hz, and an open circuit potential. The specific capacitance (C_s) of the electrode materials was derived using the equation $C_s=(I/m)/(\Delta t/\Delta V)$, where I/m, Δt, and ΔV represent the constant discharge current density, discharge time, and change in potential during discharging, respectively.

RESULTS AND DISCUSSION

We developed a template-free method of synthesizing PNT by polymerizing NT-CME4 and then using $AlCl_3$ to catalyze Friedel-Crafts-type post-crosslinking with DCE at 80 °C (Fig. 1). NT can be directly polymerized with CME in $ZnCl_2$ at some temperature [34]. We divided the procedure into two steps to prevent polymerization and further control the condensation in order to increase the surface area of the final porous carbon. The NT monomer was first chloromethylated with four equivalents of CME in $ZnCl_2$ at room temperature and was subsequently self-polymerized in $AlCl_3$ at 80 °C and calcined at 600 °C. The BET specific surface area of the PNT-C was 711.6 m^2g^{-1}. The BJH pore size distribution is shown in Fig. 2(a). The nanoporous PNT-C structure can also be categorized as (i) microporous, showing a notable peak in the range 1.1-1.7 nm; (ii) mesoporous (>2 nm); and (iii) macroporous (>50 nm). Assembling the micro-, meso-, and macropores forms the hierarchical construction, which was evidenced by the BJH pore-size distribution. Fig. 2(c) shows representative SEM images of the hierarchical carbon substrate containing 50-100-nm macropores. The TEM images clearly reveal the microporous structure (Fig. 2(d)). The results indicate that the carbon materials showed a hierarchical porous structure.

The PNT-C showed a large specific surface area and a hierarchical porous network, which will benefit for ion transfer/diffusion. The accessibility of redox molecules and ions into pores less than2nm depends on both the size of the solvated molecules and the pore diameter [35]. When the pore diameter is close to the ion size (0.5-1 nm for aqueous electrolytes), nanopores maximally contribute to the electrochemical double layer capacitor since the ions will strongly interact with the pores in the wall, leading to high electro adsorption [36]. However, the nanopores negligibly contribute to ion transport in the electrolyte. In contrast, mesopores of 2-50 nm diameter favor the rapid mass transport of ions to the electrode surface, which facilitates the charging/discharging of the electric double-layer [37].

An ideal pore structure for an SC should show a large pore volume for energy storage, a suitable ion transport channel for fast

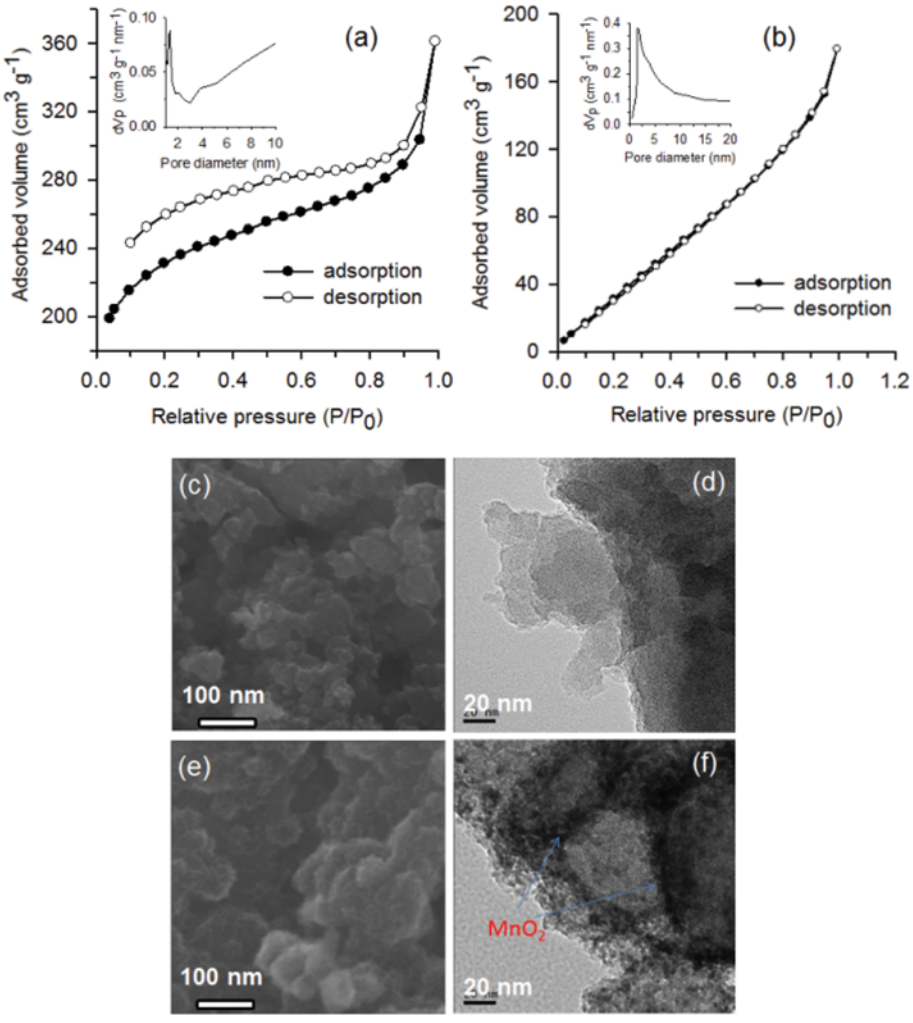

Fig. 2. Nitrogen adsorption-desorption isotherms and corresponding pore-size distribution curves (insets) of (a) hierarchical carbon substrate PNT-C and (b) C-MnO_2-120 nanocomposite, SEM (c) and TEM (d) images of as-prepared PNT-C, and SEM (e) and TEM (f) images of C-MnO_2-120.

delivery of ions into the electrode, and active pore walls for increasing the specific capacitance. Similar criteria also apply to metal oxide/carbon composite electrodes since the pseudo-capacitance of metal oxides depends on fast surface redox reactions. Hence, ion access and transport play critical roles in composite electrodes [10]. Carbon substrates with hierarchical pore support (*i.e.*, pores showing multiple-length diameters) offer tunable platforms for tailoring the fine porous microstructures and specific surface areas of C-MnO_2 electrodes. The nanocomposites were prepared by a self-limiting growth method. The MnO_2 coating was achieved by the redox reactions of $KMnO_4$ aqueous solution with sacrificed carbon substrates that contain hierarchical pores (Fig. 2(f)).

The structure and composition of the nanocomposites strongly depended on the reaction conditions. The ICP mass analysis results for the MnO_2 content of the composites synthesized for 10, 30, 60, and 120 min are shown in Fig. 3 (also in Table 2). The MnO_2 content rapidly increased to 81% within 120 min owing to the self-limiting growth mechanism. The rapid formation of MnO_2 can be attributed to the large carbon/$KMnO_4$ contact area and to rapid

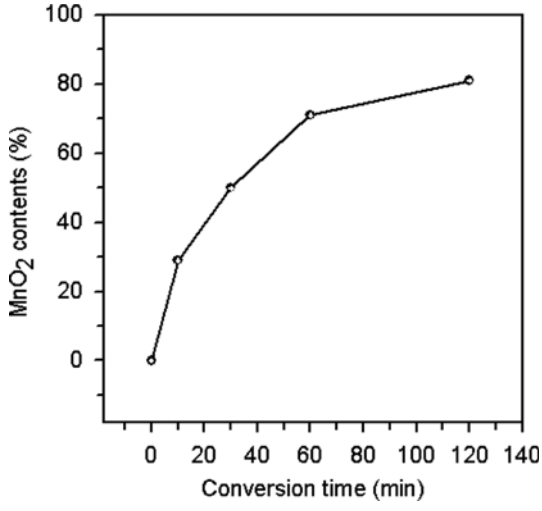

Fig. 3. Dependence of MnO_2 content on duration of reaction between carbon substrates and $KMnO_4$ solution, as measured using ICP mass analysis.

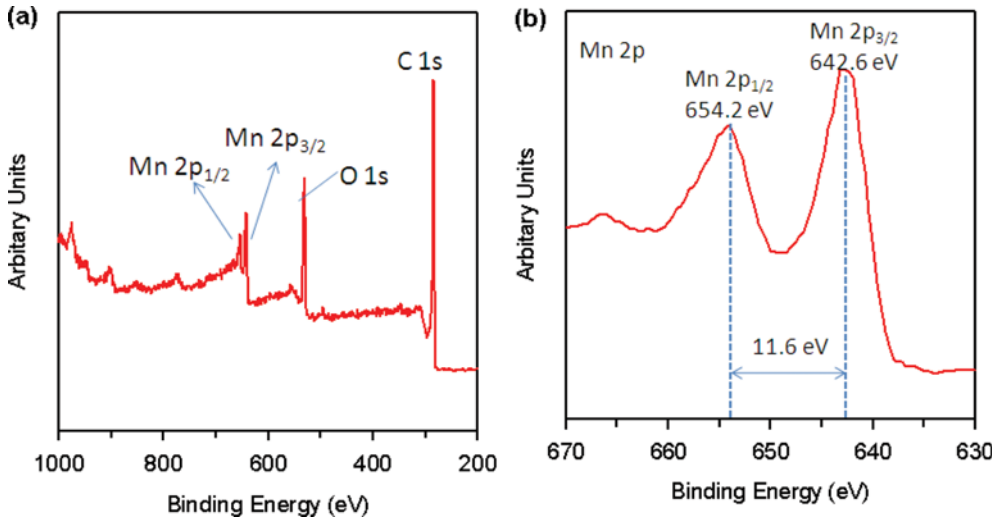

Fig. 4. XPS spectra for C-MnO_2: (a) Wide-scan survey spectra for C-MnO_2 and (b) narrow spectra for Mn 2*p* peaks attributable to C-MnO_2 composite.

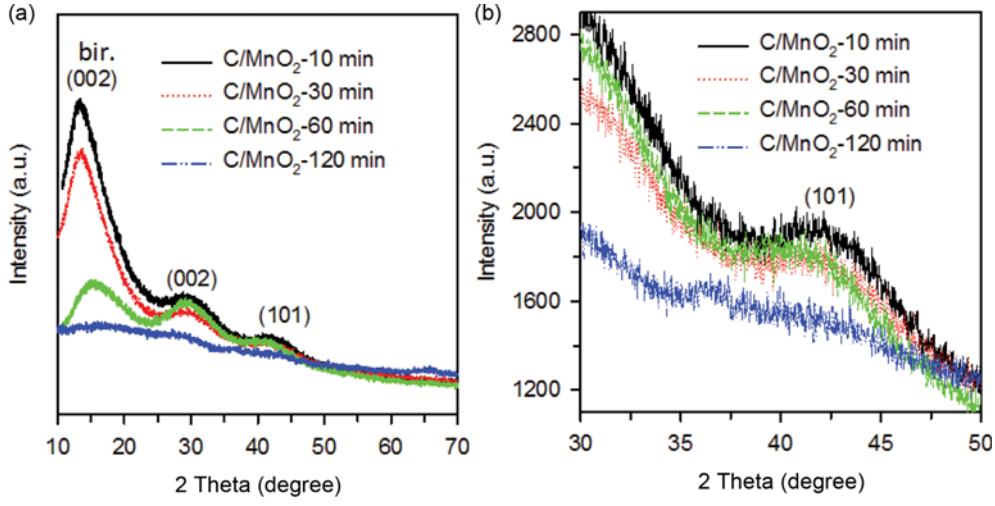

Fig. 5. High-angle XRD patterns of C-MnO_2 (bir.:birnessite) (a) with their expanded peaks at 42° (b).

$KMnO_4$ diffusion and reaction kinetics [20].

The XPS results, indicating the formation of C-MnO_2 on the carbon surfaces and edges, are presented in Fig. 4, which shows the C-MnO_2 survey and the deconvoluted Mn 2*p* core-level spectra for C-MnO_2. The C-MnO_2 survey spectrum only shows signals corresponding to C, O, and Mn $2p_{3/2}$ and $2p_{1/2}$, implying MnO_2 that nanoparticles had formed on the carbon surface. The deconvoluted Mn 2*p* core-level spectrum for C-MnO_2 shows the Mn $2p_{3/2}$ and $2p_{1/2}$ peaks centered at 642.6 and 654.2 eV, respectively. Although the peak positions are slight different, the Mn $2p_{3/2}$ and $2p_{1/2}$ peaks are consistently separated by a spin energy of 11.6 eV. These results are also consistent with previously reported data for the Mn $2p_{3/2}$ and Mn $2p_{1/2}$ peaks attributable to MnO_2 nanoneedles [33].

Figs. 2(e) and (f) show the FE-SEM and TEM images of the C-MnO_2-120, respectively. Compared to the corresponding images in Figs. 2(c) and (d), these show that the MnO_2 clearly homogeneously decorated the carbon surface, suggesting that the MnO_2 in the composites was polycrystalline, which was further evidenced using XRD (Fig. 5). The XRD pattern showed an obvious sharp peak, marked "bir." (birnessite), characteristic of δ-MnO_2 [38] at 2θ=12.8° (002), which can be assigned to Na-bir. However, the peak intensity spontaneously decreased with increasing reaction time. There are no obvious MnO_2 diffraction peaks in the high-angle X-ray diffraction patterns for C-MnO_2-120, owing to the amorphous reduced products.

The pore structure of the nanocomposites was also determined using nitrogen sorption (Table 2). Fig. 2(b) shows the different nitrogen sorption isotherms and pore size distributions of the C-MnO_2-120. The uptake at a low relative pressure was significantly lower, suggesting a reduced microporosity and mesoporosity. The uptake at a higher relative pressure (P/P_0), however, suggested that the macroporosity was retained.

Synthesizing C-MnO_2 nanocomposites with hierarchical porous networks and tunable oxide contents provides unique materials for studying pseudo-capacitance. The SC electrodes have been fabricated with the samples and characterized them using CV and gal-

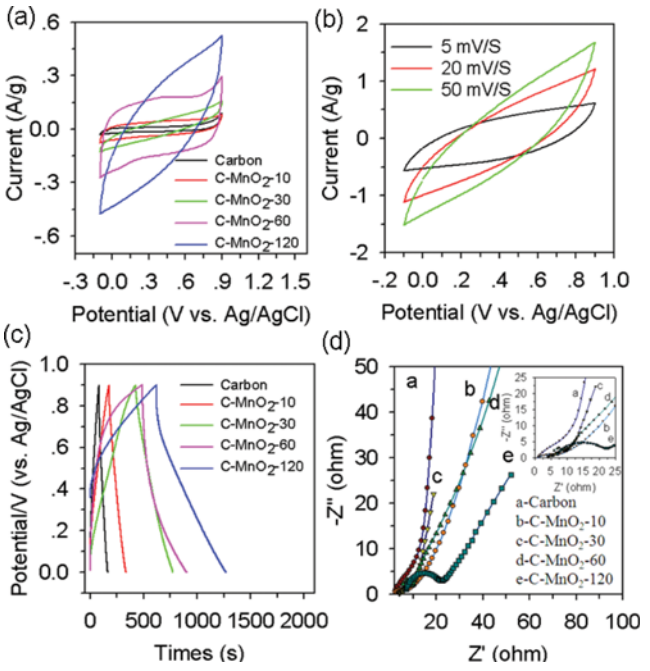

Fig. 6. CV curves for (a) carbon and hybrid electrodes scanned at 5 mV s^{-1} and (b) C-MnO_2-120 scanned at different rates in 1 M aqueous Na_2SO_4; (c) Galvanostatic charge/discharge curves for carbon and C-MnO_2 electrodes measured in 1 M aqueous Na_2SO_4 solution between 0 and 0.9 V at 1.0 A g^{-1}; (d) Nyquist plots from impedance spectroscopic analysis of carbon and C-MnO_2 composite electrodes with inset showing expanded high-frequency region of plots.

vanostatic charge/discharge measurements. Fig. 6(a) shows the CV curves for the carbon, C-MnO_2-10, C-MnO_2-30, C-MnO_2-60, and C-MnO_2-120 electrodes scanned at 5 mV s^{-1} in 1 M aqueous Na_2SO_4. All of the CV curves are almost ideally rectangular, indicating that the composites showed ideal capacitive behavior. The CV curves for all of the C-MnO_2 electrodes clearly showed much larger integrated areas than that for the carbon substrate, indicating the excellent electrochemical performance of the former. Thus, it is reasonable to infer that the capacitive contribution was predominantly from the active MnO_2 electrode. Broad Faradaic peaks are observed in the composites electrode during CV scan in Na_2SO_4 aqueous electrolyte, due to the fact that the MnO_2 act as the redox centers [10]. The C-MnO_2 electrode obviously also showed increasing polarization, believed to be due to the increased electron and transport resistance, with increasing MnO_2 content. Nevertheless, the specific capacitance increased to 286.8 F g^{-1} when the mass loading was 81% MnO_2 (C-MnO_2-120). More importantly, the shape of the CV curves for the MnO_2 hybrid electrode tended to deviate from the ideal rectangle at high scan rates, as shown in Fig. 6(b), which is mainly attributable to the sluggish incorporation of ions into the active electrode material because only the outer surface or subsurface was used for charge storage [39].

The composite electrodes also demonstrated distinct galvanostatic charge/discharge behaviors. The carbon, C-MnO_2-10, C-MnO_2-30, C-MnO_2-60, and C-MnO_2-120 electrodes were measured in 1 M aqueous Na_2SO_4 at a current density of 1.0 A g^{-1}. As illustrated in Fig. 6(c), the charge curves for all the electrodes were almost symmetric to their corresponding discharge counterparts but for some curvature during charging and discharging, indicating pseudo-capacitive and double layer contributions. The C-MnO_2 electrodes exhibited longer discharge increasing with the denoted time, which are consistent with the specific capacitance behavior since discharging is directly proportional to the specific capacitance of an electrode [40].

Nyquist plots, in which impedance is plotted as a function of frequency, have often been used to evaluate conductivity and ion diffusion in the electrode/electrolyte. The $-Z''$ axis is usually referred to as the capacitive parameter and the real component, Z' axis referred to as the ohmic parameter. The signal penetrates progressively deeper inside the porous structure of the electrode when the frequency decreases from very high frequencies, enabling more and more of the electrode surface to become available for ion adsorption. The mid-frequency range is related to the electrolyte penetration inside the porous structure of the highly porous electrodes, and this region is usually called the Warburg curve [41].

Fig. 6(d) shows Nyquist plots for the carbon substrate and composite electrodes prepared with different oxide content, all of which show comparable ohmic resistances. All the composite electrode impedance plots showed a semicircle in the mid-frequency region and a nearly vertical line in the low-frequency region. The intersection of the semicircle with the Z' axis refers to the equivalent series resistance (R_s) of the electrode, and the diameter of the semicircle corresponds to the charge-transfer resistance (R_{ct}) of the electrode-electrolyte interface [43]. The R_s for the carbon, C-MnO_2-10, C-MnO_2-30, C-MnO_2-60, and C-MnO_2-120 electrodes (obtained from the Z'-intercept of the Nyquist plot in Fig. 6(d)) were 0.94, 6.26, 9.10, 9.34, and 22.06 Ω, respectively (Table 2). The C-MnO_2-120 electrode showed the highest R_{ct} because it showed the highest MnO_2 content, leading to low conductivity at the electrode-elec-

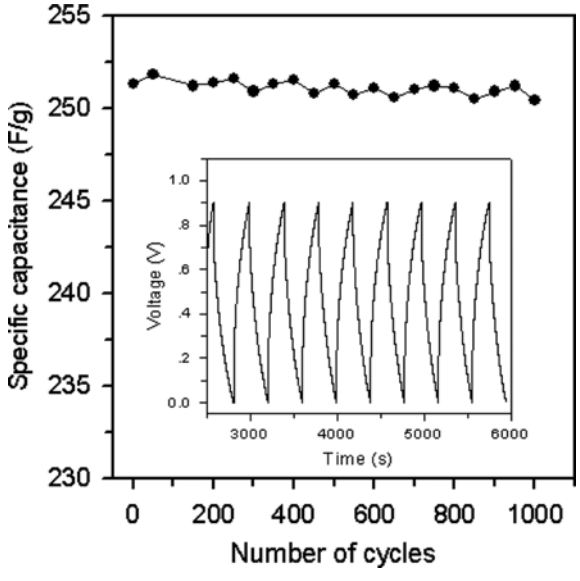

Fig. 7. Cycling stability and typical charge/discharge curves (insert) for C-MnO_2-120 nanocomposite measured at room temperature and 100 mAg^{-1} in 1 M aqueous Na_2SO_4.

trolyte interface.

Besides the outstanding capacitance, the C-MnO_2 composite endows the nanocomposites with long cycling stability. Fig. 7 shows the specific capacitance of the C-MnO_2-120 electrode repeatedly charged/discharged at a constant 100 mAg^{-1} in 1 M aqueous Na_2SO_4. The cycling performance is shown in the insert. The electrode retained a very stable capacitance over 1000 cycles, suggesting good electrochemical cycling stability.

CONCLUSIONS

We have developed a template-free method of fabricating 3-D carbon substrates, whose large surface areas and hierarchical structures not only physically support metal oxides but also provide channels for charge transport. Self-limiting growth was used to synthesize a hybrid-structured controllable MnO_2 loading on the 3-D carbon substrate surface as a high-performance *pseudo*-capacitor electrode. The novel hierarchical carbon-MnO_2 composite architecture clearly reduced the resistance to charge transfer and ion diffusion, demonstrating a high areal capacitance and long cycling stability. The composite electrode shows some potential applications for the development of high-performance SC in a wide range of fields.

ACKNOWLEDGEMENTS

This work was supported by a 2-Year Research Grant of Pusan National University. The authors also thank the BK21 PLUS Program for partial financial support.

REFERENCES

1. P. Simon and Y. Gogotsi, *Nat. Mater.*, **7**, 845 (2008).
2. P. J. Hall, M. Mirzaeian, S. I. Fletcher, F. B. Sillars, A. J. R. Rennie, G. O. Shitta-Bey, G. Wilson, A. Cruden and R. Carter, *Energy Environ. Sci.*, **3**, 1238 (2010).
3. L. Yang, S. Cheng, Y. Ding, X. Zhu, Z. L. Wang and M. Liu, *Nano Lett.*, **12**, 321 (2011).
4. M.-K. Song, S. Cheng, H. Chen, W. Qin, K.-W. Nam, S. Xu, X.-Q. Yang, A. Bongiorno, J. Lee and J. Bai. *Nano Lett.*, **12**, 3483 (2012).
5. J. Y. Kim, S.-H. Lee, Y. Yan, J. Oh and K. Zhu, *RSC Adv.*, **2**, 8281 (2012).
6. V. Aravindan, Y. L. Cheah, W. F. Mak, G. Wee, B. V. R. Chowdari and S. Madhavi, *ChemPlusChem*, **77**, 570 (2012).
7. H.-C. Chien, W.-Y. Cheng, Y.-H. Wang and S.-Y. Lu, *Adv. Funct. Mater.*, **22**, 5038 (2012).
8. Y. Wang, Z. Hong, M. Wei and Y. Xia, *Adv. Funct. Mater.*, **22**, 5185 (2012).
9. K. Liang, X. Tang and W. Hu, *J. Mater. Chem.*, **22**, 11062 (2012).
10. M. Zhi, C. Xiang, J. Li, M. Li and N. Wu, *Nanoscale*, **5**, 72 (2013).
11. A. S. Aricò, P. Bruce, B. Scrosati, J. M. Tarascon and W. Van Schalkwijk, *Nat. Mater.*, **4**, 366 (2005).
12. X. Xia, J. Tu, Y. Zhang, X. Wang, C. Gu, X. B. Zhao and H. J. Fan, *ACS Nano*, **6**, 5531 (2012).
13. A. L. M. Reddy, S. R. Gowda, M. M. Shaijumon and P. M. Ajayan, *Adv. Mater.*, **24**, 5045 (2012).
14. W.-S. Kim, Y. Hwa, J.-H. Shin, M. Yang, H.-J. Sohn and S.-H. Hong, *Nanoscale*, **6**, 4297 (2014).
15. C. Yuan, L. Zhang, L. Hou, G. Pang and W.-C. Oh, *RSC Adv.*, **4**, 14408 (2014).
16. A. Ehsani, B. Jaleh and M. Nasrollabzadeh, *J. Power Sources*, **257**, 300 (2014).
17. A. Bordes, K. S. Eom and T. F. Fuller, *J. Power Sources*, **257**, 163 (2014).
18. Z. Qian, T. Peng, L. Qu, J. Wang and P. Wang, *J. Mater. Chem. A*, **2**, 4894 (2014).
19. L. Wang, C. Lin, F. Zhang and J. Jin, *ACS Nano*, **8**, 3724 (2014).
20. Y. Peng, Z. Chen, J. Wen, Q. Xiao, D. Weng, S. He, H. Geng and Y. Lu, *Nano Res.*, **4**, 216 (2011).
21. A. E. Fischer, K. A. Pettigrew, D. R. Rolison, R. M. Stroud and J. W. Long, *Nao Lett.,* **7**, 281 (2007).
22. W.-H. Qu, F. Han, A.-H. Lu, C. Xing, M. Qiao and W.-C. Li, *J. Mater. Chem. A*, **2**, 6549 (2014).
23. A. Gambou-Bosca and D. Bélanger, *J. Mater. Chem. A*, **2**, 6463 (2014).
24. S. Cheng, L. Yang, Y, Lin, W. Lin, L. Huang, D. Chen, C. P. Wong and M. Liu, *J. Mater. Chem. A*, **1**, 7709 (2013).
25. M. Minakshi, D. Meyrick and D. Appadoo, *Energy Fuels*, **27**, 3516 (2013).
26. H. Wang, Z, Xu, Z. Li, K. Cui, J. Ding, A. Kohandehghan, X. Tan, B. Zahiri, B. C. Olsen, C. M. B. Holt and D. Mitlin, *Nano Lett.*, **14**, 1987 (2014).
27. Q. H. Do, J. Smithyman, C. Zeng, C. Zhang, R. Liang and J. P. Zheng, *J. Power Sources*, **248**, 1241 (2014).
28. S.-B. Yoon and K.-B. Kim, *Electrochim. Acta,* **106**, 135 (2013).
29. W. Wei, X. Cui, W. Chen and D. G. Ivey, *Chem. Soc. Rev.*, **50**, 1697 (2011).
30. Y. Meng, W. Song, H. Huang, Z. Ren, S.-Y. Chen and S. Suib, *J. Am. Chem. Soc.*, **136**, 11452 (2014).
31. X. Zhang, Q. Jin, L. Dai and S. Yuan, *Bull. Mater. Sci.*, **34**, 735 (2011).
32. M. Wu, G. A. Snook, G. Z. Chen and D. Fray, *J. Electrochem. Commun.*, **6**, 499 (2004).
33. M. Kim, Y. Hwang, K. Min and J. Kim, *Phys. Chem. Chem. Phys.*, **15**, 15602 (2013).
34. X. H. Huang, S. Kim, M. S. Heo, J. E. Kim, H. Suh and I. Kim, *Langmuir*, **29**, 12266 (2013).
35. J. H. Bae, J.-H. Han and T. D. Chung, Electrochemistry at nanoporous interfaces: new opportunity for electrocatalysis. *Phys. Chem. Chem. Phys.*, **14**, 448 (2012).
36. E. Raymundo-Piñero, K. Kierzek, J. Machnikowski and F. Béguin, *Carbon*, **44**, 2498 (2006).
37. G. Gryglewicz, J. Machnikowski, E. Lorenc-Grabowska, G. Lota and E. Frackowiak, *Electrochim. Acta*, **50**, 1197 (2005).
38. V. V. Vol'khin, O. A. Pogodina and G. V. Leont'eva, *Russ. J. Gen. Chem.*, **72**, 173 (2002).
39. G. Yu, L. Hu, M. Vosgueritchian, H. Wang, X. Xie, J. R. McDonough, X, Cui, Y. Cui and Z. Bao, *Nano Lett.*, **11**, 2905 (2011).
40. M. Kim, Y. Hwang and J. Kim, *J. Power Sources*, **239**, 225 (2013).
41. Q. Cheng, J. Tang, J. Ma, H. Zhang, N. Shinya and L.-C. Qin, *Carbon*, **49**, 2917 (2011).